



# Additive manufacturing of AISI 420 stainless steel: process validation, defect analysis and mechanical characterization in different process and post-process conditions

Erica Liverani<sup>1</sup> · Alessandro Fortunato<sup>1</sup>

Received: 4 March 2021 / Accepted: 2 July 2021 / Published online: 2 August 2021  
© The Author(s) 2021

## Abstract

Stainless steel (SS) alloys produced by laser-based powder bed fusion (LPBF) offers comparable and sometime superior mechanical properties compared to conventionally processed materials. Some of these steels have been extensively studied over the last decade; however additively manufactured martensitic SS, such as AISI 420, need further research in characterizing their post-built quality and mechanical behaviour. This lack of information on martensitic SS is not consistent with their growing demand in the automotive, medical and aerospace industries due to their good corrosion resistance, high hardness and good tensile properties. Selection of the appropriate process parameters and post treatments plays a fundamental role in determining final properties. For this reason, the effect of LPBF process parameters and different heat treatments on density, defect characteristics and locations, roughness and mechanical properties of AISI 420 were investigated in this paper. A first experimental campaign was carried out to establish a set of suitable process parameters for industrial applications. Starting from this result, detected defect properties were investigated by computed tomography (CT) scans. Dimensions, sphericity and distributions of defects inside the volume were analysed and compared between samples manufactured with different parameters. In the second part of the paper, the influence of process and post-process conditions on mechanical properties was investigated. The final presented results establish a correlation between the employed production cycle and the resulting properties of LPBF AISI 420 specimens.

**Keywords** Additive manufacturing · Laser powder bed fusion · Martensitic stainless steel · Defects · Mechanical properties · Heat treatment

## 1 Introduction

Stainless steel (SS) alloys are used in a growing number of industrial applications due to their high strength, toughness and good or excellent corrosion resistance. Austenitic or ferritic SS are preferred in highly corrosive environments such as those within chemical, petrochemical, marine and medical applications, while martensitic SS is used when good mechanical properties are also required. Strength and toughness of martensitic SS can be

tailored through an appropriate heat treatment [1] making these steels particularly interesting for applications in extraction, oil and gas and tool industries.

These alloys can be processed by different conventional manufacturing processes such as casting, metal forming and powder metallurgy or, more recently, additive manufacturing (AM). Among all alloys proposed by powder manufacturers and retailers for AM metal processes, some SS are well studied in literature, including AISI 316L or AISI 304, thanks to their increasing expansion in the market and aptitude for printing. A lack of knowledge is instead evident in the case of martensitic SS [2], such as AISI 420, due to the fact that their chemical composition is less suitable for AM optimization, which induces melting and high-speed re-solidification of the raw material. However, comparing the mechanical properties of AISI 420 bars in the pre-hardened and tempered condition with as-built components obtained by AM

---

✉ Erica Liverani  
erica.liverani2@unibo.it

<sup>1</sup> Department of Industrial Engineering (DIN), Alma Mater Studiorum - University of Bologna, Viale Risorgimento 4, 40136 Bologna, Italy

processes, the improvement is not negligible. Cold drawn conventional samples have a yield strength of around 590 MPa [3], while AM components can reach 1000 MPa [4]. This difference is because AISI 420 responds to heat treatments similarly to construction steels. The thermal cycle experienced by martensitic SS during AM, in fact, induces the formation of quenched martensite [5] responsible for increases in hardness and strength and a reduction in ductility. The high amount of carbon, however, decreases the alloy's corrosion resistance and weldability. The latter aspect makes AISI 420 more complex than austenitic SS to optimize for AM due to the easy occurrence of cracks during the re-solidification phase of each layer. Furthermore, considering the industrial applications of martensitic SS, one of the advantages of using AM could be to fabricate near-net-shape parts, such as con-formal channels for dies and tools, to directly implement into service without additional processing steps. However, the typical surface roughness of as-built AM parts has proven to be higher than conventional processes [6], and subsequent finishing processes are often difficult to apply [7]. The high roughness is caused by several processing characteristics such as process parameters, sintered powder particles on the surface and the natural stair-step effect of layer manufacturing [8]. All of the involved parameters must be optimized to reduce the initial roughness and improve the surface quality of as-built components.

Taking into account the specific AM process used for AISI 420 production, several papers have been published using direct energy deposition (DED) [4, 9], and only more recently some authors approached these steels using laser-based powder bed fusion (LPBF). In particular, Zhao et al. [10] studied the effect of LPBF parameters on the density and mechanical properties of AISI 420. Saiedi et al. [11] instead focused their work on differences in microstructure between as-built and tempered AISI 420 components and the effect of post-processes on tensile behaviour, starting from one predetermined set of LPBF process parameters. Nath et al. [12] defined a relationship between the microstructure, mechanical properties and corrosion behaviour of LPBF 420 steel. Finally, a more complete work on microstructural characterization and texture evolution of AISI 420 was proposed by Tian et al. [13]. An optimized 3-step heat treatment (austenitization at 1043 °C for 1 h followed by nitrogen quenching and double tempering at 182 °C with 3 h soaking time and final air cooling) was presented to obtain a fully martensitic phase with carbide precipitation that produced a significant increase in yield strength.

Despite the interesting results obtained in these works, more effort is necessary to identify the correlation between LPBF parameters and final component characteristics both in terms of defects and mechanical properties, together with the effect of different heat treatments on the same properties. In particular, while the effects of

microstructure on mechanical properties is partially known from studies performed on conventionally manufactured AISI 420, LPBF defects and their correlation with the mechanical properties have seen little investigation. As is well known, fatigue failure and corrosion phenomenon, both of great importance for martensitic SS, are strongly influenced by the existence of these defects [14, 15], and LPBF process parameters and variations in the production chamber all affect the final defect content and performance of components [16].

In response to this lack of information, this study investigates the performance of LPBF AISI 420 samples produced with three different sets of parameters established based on three specific industrial criteria: (1) higher density with process stability for large component production, (2) acceptable density associated with high speed, and (3) surface defect and roughness reduction for improvement of fatigue and corrosion resistance. The variables under consideration include process parameters such as scanning strategy, laser speed, build orientation and layer thickness. By varying the above parameters, component quality in terms of number, size and geometry of defects, sample hardness, roughness and mechanical behaviour was analysed. Moreover, the performance of as-built components was compared to heat-treated samples. Two bulk industrial thermal treatments were chosen and the results are compared to laser hardening performance in terms of hardness. Surface hardening, in fact, is usually used to improve tribological properties such as corrosion, wear and hardness [17] that are of particular importance for AISI 420 SS.

## 2 Materials and methods

### 2.1 Sample production and post-processes

Atomized 420 SS powder supplied by Ridix (RIDIX S.p.A., Grugliasco, Italy), with nominal chemical composition as reported in Table 1, was used to produce LPBF samples for microstructural and mechanical characterization. All samples were fabricated with a commercial LPBF system equipped with a 1070 nm fibre laser (Concept Laser M2) with a maximum power of 370 W.

**Table 1** Nominal chemical composition of AISI 420 steel powder [wt%]

Cr	Mn	Si	C	P	S	N	O	Fe
12–14	0–1	0–1	0.15–0.40	≤0.04	≤0.03	0.1	0.1	Balance

The unit had a build envelope of 250 × 250 × 280 mm (x, y, z), and the build platform was not pre-heated.

All samples were built in an argon environment with a residual oxygen content of 0.1%. Process parameters and scanning strategy were defined using the machine control software, while component orientation and support generation were designed by the dedicated software Magics (Materialise, Leuven, Belgium). A rotating 5 × 5 mm<sup>2</sup> chessboard scanning strategy was utilized to melt the bulk volume with alternating parallel line laser movement applied within each square, with the overlap defined in the experimental campaign.

A preliminary study was performed to investigate the process parameter window that enabled the fabrication of components that met the three criteria described in the introduction. For this purpose, 10 × 10 × 15 mm<sup>3</sup> samples were printed, and the following process parameters changed: scan speed, spot size, hatch distance and layer thickness.

More than 40 combinations of parameters achieving energy density (defined in Equation 1) in the range 30–205 J/mm<sup>3</sup> were tested (Table 2). Power was fixed at 370 W for all samples.

$$E = \frac{P [W]}{v \left[ \frac{mm}{s} \right] \cdot l [\mu m] \cdot h [\mu m]} \tag{1}$$

where P is the laser power; v is the laser scan speed; l is the layer thickness; and h is the hatch distance.

Density measurements were carried out on these samples as described in the following section.

Two sets of parameters responding to criteria 1 and 2 were defined, and 32 tensile samples for subsequent mechanical characterization were produced based on these preliminary results (4 for each condition). LPBF parameters (OP=optimized parameters), together with build direction (BD), are shown in Table 3. After the building process, 8 samples of the OP1\_90 series were subject to two different post-heat treatments (4 samples for each).

**Table 2** LPBF process parameters used to identify the optimal printing condition

Spot size [μm]	Scan speed [mm/s]	Hatch distance [μm]
Parameters for criteria 1 and 2 (layer thickness = 50 μm)		
120	From 900 to 1600	127.5-112.5-75
100		112.5-75-60
80		112.5-75-45
Parameters for criteria 3 (layer thickness = 30 μm)		
120	800-1400	50
100	800–1800	

**Table 3** LPBF process parameters used for manufacturing of tensile specimens

Series	Spot size [μm]	Scan speed [mm/s]	Hatch distance [μm]	BD [°]
OP1-90	120	1200	75	90
OP1-45	120	1200	75	45
OP1-0	120	1200	75	0
OP2-90	100	1600	75	90
OP2-45	100	1600	75	45
OP2-0	100	1600	75	0

Lathe finishing operations were foreseen to reduce the roughness of the LPBF tensile samples to 12 μm.

Subsequently LPBF process parameters were selected for criteria 3 improvement (OP3), and the manufacturing of “skin and core” samples was carried out for density and roughness analysis. Skin and core samples were prepared using OP1 in the core and OP3 for a 2 mm skin layer (Table 4).

**2.2 Post-heat treatment conditions**

The investigated bulk heat treatment conditions used for mechanical property enhancement were the following:

- QT (quenching and tempering): heating up to 780 °C (10°C/min) with 45-min soaking time followed by heating up to 1050 °C (10°C/min) with 1-h soaking time. Cooling of the samples to room temperature in a nitrogen environment at 5000 mbar. Final tempering at 230 °C for 2 h
- N (normalization) + QT: heating up to 900 °C (10°C/min) with 90-min soaking time followed by a cooling in oven to 580 °C followed by a cooling to room temperature in a nitrogen environment at 1000 mbar + QT

In order to give an assessment of the effect of laser hardening on AISI 420 manufactured with LPBF, preliminary tests were performed on as-built parallelepiped components of dimensions 80 mm × 80 mm × 10 mm. Single traces aligned and spaced 10 mm from each other were performed on each

**Table 4** Process parameters for surface defect and roughness reduction

Core		OP1
Skin	Power [W]	370
	Scan speed [mm/s]	1400
	Layer thickness [μm]	30
	Hatch distance [μm]	75
	Spot diameter [μm]	100

**Table 5** Process parameters used for laser surface hardening

Tests	Laser speed [mm/s]	Laser power [W]
1–5	2	400–800
6–11	4	600–1100

sample, varying the laser power and speed as shown in Table 5. All tests were carried out using a 3.3 kW diode laser with a wavelength of 930 nm and a 150 mm focusing lens achieving a 6 mm × 6 mm top-flat spot.

### 2.3 Density measurements and defect investigation

The process parameters shown in Table 2 were initially evaluated with density tests. A Radwag balance (Type PS600 R2) with a specific density measurement device for solid materials and a measurement accuracy of 0.001 g was firstly used as a non-destructive method based on Archimedes' principle. The relationship between density and process parameters was defined and OP1 and OP2 selected for subsequent tests. Archimedes' density measurements were then integrated with computed tomography (CT) analysis. The main advantage of CT over conventional weighing and optical techniques is its capability of performing non-destructive measurement of the external and internal micro-features (including defects) [18]. Furthermore, defect characteristics such as size, shape, location and distribution can be evaluated [19], representing important information to respond to the requests of LPBF component quality.

In this work, CT measurements were performed on selected samples (printed with OP1, OP2 and OP3) of size 6×6×8 mm<sup>3</sup> with a CT scan system (Nikon XT H 225 ST). The X-ray tube voltage was set at 233 kV, the current at 0.5 mA and the exposure time at 2.83 s, achieving an approximate voxel size of 11 μm. Data processing was carried out using VGStudio MAX 3 (Volume Graphics GmbH, Germany) software, and void analysis was performed with the VGDefX defect detection algorithm.

Together with the final volume density of the samples, defect analysis was carried out in order to identify the main defect categories and their spatial distribution. The defect characteristics gathered from CT analysis included diameter, sphericity and projected area on three orthogonal planes (perpendicular and parallel to the build direction). The defect diameter means the diameter of the circumscribed sphere of the defect, while the sphericity corresponds to the ratio between the surface of a sphere with the same volume as the defect and the surface of the defect. The sphericity ranges between 0 and 1, where 1 represents a perfect sphere.

### 2.4 Microstructural characterization

Microstructural characterization for defect detection and correlation with CT results was carried out with an optical microscope (OM, Nikon Optiphot-100) both on preliminary samples and tensile specimens. Representative as-built and heat-treated samples were longitudinally and transversely sectioned and prepared according to standard metallographic techniques comprising mechanical grinding (80–2000 grit papers) and polishing with alumina in suspension down to a particle size of 0.6 μm. In order to reveal microstructural features, the samples were etched using a Vilella reagent (10 ml HNO<sub>3</sub>, 30 ml HCl, 30 ml glycerine).

### 2.5 Surface quality

Surface roughness of all initial 10 × 10 × 15 mm<sup>3</sup> AISI 420 samples was measured with a stylus profilometer (Alpa RT-25; tip radius = 5 μm) orthogonally to the building direction. A minimum of 5 measurements were carried out on two distinct faces of each sample as shown in Fig. 1. The main values and their correlation with process parameters guided definition of the aforementioned skin parameters (see Table 4). The roughness measurements of optimized skin and core samples were carried out with the same equipment.

### 2.6 Mechanical characterization

The influence of process parameters, orientation and heat treatment on the mechanical properties was determined with tensile tests and hardness measurements. The experimental campaign was carried out on circular cross sections in accordance with standards (ISO 6892-1 [20]): 30 mm gauge length and 6 mm in diameter. Tensile tests were performed with a servo hydraulic press (Italsigma, Forlì, Italy) equipped with a 100 kN load cell and an extensometer with a gauge length of 20

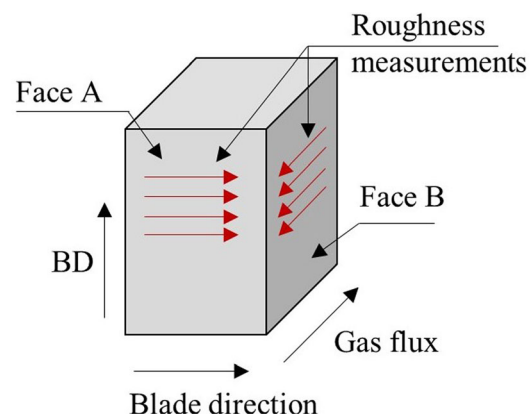


**Fig. 1** Roughness measurement for the surface quality

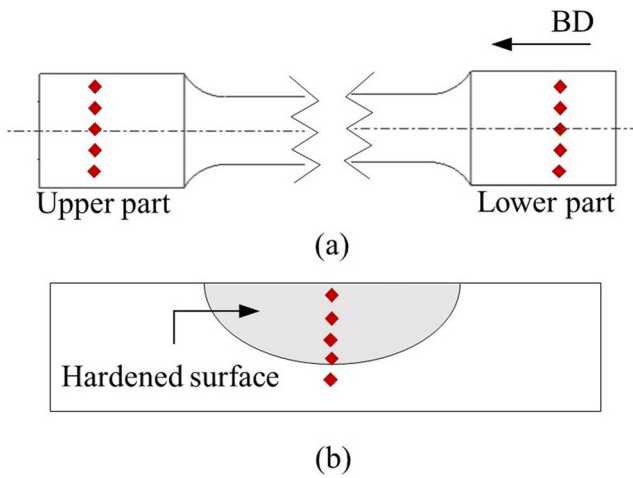


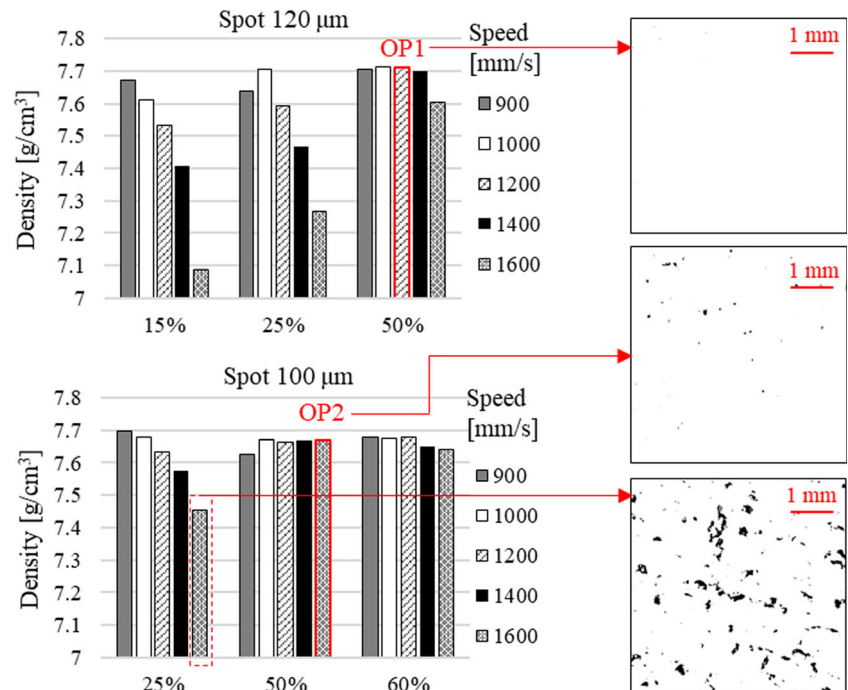
Fig. 2 Microhardness tests on tensile samples (a) and laser hardened parallelepipeds (b)

mm. The strain rate was set to  $5 \cdot 10^{-4} \text{ s}^{-1}$  and maintained fixed using a constant cross-head separation rate of 1 mm/min.

Vickers microhardness tests were performed using a 0.5 kg load (HV0.5) and a 10 s dwell time on metallographic samples, cut from both the upper and lower part of tensile specimens (Fig. 2a), to assess the effects of post-heat treatments on microstructure evolution.

Furthermore, HV1 measurements were carried out on laser-treated samples in order to identify the hardening depth (Fig. 2b) and the maximum hardness. These latter results were compared with hardness measurements performed on as-built and conventionally heat-treated samples.

Fig. 3 Influence of process parameters on the final density and selection of optimized sets enabling the production of high-density samples. Low magnification micrographs of three representative conditions are shown on the right.



### 3 Results

#### 3.1 Process parameter definition

Fig. 3 shows the process parameter combinations that allowed identification of the highest densities ( $\rho$ ). It was found that components characterized by  $\rho > 7.65 \text{ g/cm}^3$  could only be produced with energy density up to  $62 \text{ J/mm}^3$ . Exceeding this threshold, the single parameters involved influenced the final results according to the following considerations:

- Power densities ( $P/\text{spot area}$ ) obtained with the maximum output power (370 W) and a spot diameter of  $120 \mu\text{m}$  are sufficient for complete layer melting only for higher interaction time between the laser source and powder bed, therefore for laser speed less than or equal to  $1200 \text{ mm/s}$ . These parameters returned the highest density values for a hatch distance of  $75 \mu\text{m}$ . For smaller hatch distances, the melt pool does not correctly melt all the volume, leaving unmelted areas between adjacent traces, in particular as the scan speed increases.
- Tests conducted with a spot size of  $100 \mu\text{m}$  showed a density development less affected by laser speed both for  $75 \mu\text{m}$  and  $60 \mu\text{m}$  hatch distances. Despite the final density being slightly lower than previous results, the best compromise between final density and process velocity could be reached adopting a hatch distance of  $75 \mu\text{m}$  with a laser speed of  $1600 \text{ mm/s}$ .
- With a spot size of  $80 \mu\text{m}$  in diameter, no advantage was found with respect to the defined criteria.

**Table 6** Optimized process parameters identify with the preliminary experimental campaign.

OP	Spot size [ $\mu\text{m}$ ]	Scan speed [mm/s]	Hatch distance [ $\mu\text{m}$ ]	Layer thickness [ $\mu\text{m}$ ]
OP1	120	1200	75	50
OP2	100	1600	75	50
OP3	100	1400	75	30

The optimized process parameters, selected at the end of this experimental campaign to achieve criteria 1 and 2, are reported in Table 6 and highlighted in Fig. 3 with red contours. OP1 returned the highest density, together with the other two sets of parameters shown in Fig. 3. The final choice was made considering, as a second selection criterion, the scanning speed. OP2, on the other hand, was chosen by focusing the results on the high-speed criterion and using the density as a second output of interest.

In relation to the samples printed with a layer thickness of 30  $\mu\text{m}$ , these exhibited density values in the range of 7.68–7.72  $\text{g}/\text{cm}^3$ . This result was crossed with the roughness measurements obtained for all cited samples, with the analysis shown in Fig. 4.

The OP3 set identified for the reduction roughness is marked with a red circle, achieving a density of 7.715  $\text{g}/\text{cm}^3$ .

Skin and core samples were printed using OP1 and OP3 (as shown in Table 4) for a more in-depth analysis. Results in terms of surface defects are visible in Fig. 5, where the red dotted lines highlight a decrease in surface defects due to the skin layer. The density of the two parts measured by image analysis was 99.95% and 99.45%, respectively, for the skin and core areas.

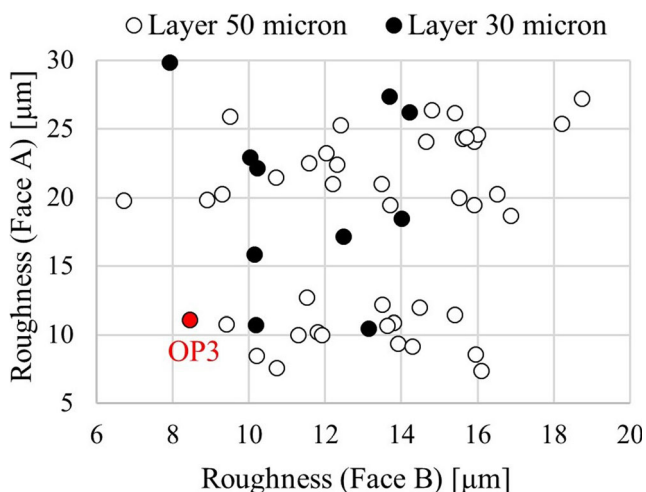


**Fig. 4** Mean roughness results obtained for all samples built in the preliminary campaign

In relation to the roughness, the mean measured values (and standard deviations) were 8.3  $\mu\text{m}$  (1.1) and 9.2  $\mu\text{m}$  (1.9), respectively, on face B and face A, in line with results in the literature for different materials [21, 22]. The OP3 set was then chosen to meet criterion 3 and added to Table 6.

OP1, OP2 and OP3 were finally used for the production of samples subject to computed tomography. CT scans returned, respectively, a defect volume ratio of 0.1%, 0.37% and 0.09% (Fig. 6). These percentages allowed definition of a density reference value of 7.72  $\text{g}/\text{cm}^3$ .

### 3.2 Defect investigation

A more in-depth data analysis of CT measurements was carried out for OP1 and OP3 LPBF samples.

Looking at Fig. 7, it is possible to state that 50% of the defects have diameters less than 0.140 mm for OP1 and less than 0.125 mm for OP3. Considering 90% of voids, these values increase up to 0.250 mm and 0.185 mm, respectively, for OP1 and OP3. Unfortunately, defects smaller than 0.05 mm could not be observed in the 3D analysis due to resolution limits (11  $\mu\text{m}$ ), as each defect needed to contain at least 3 voxels to be detected reliably.

Considering the sphericity of the defects with respect to their diameter (Fig. 8), two main categories of defects can be recognized: circular/spherical defects and elongated narrow defects.

Comparing the diameters and the sphericity of OP1 and OP3 voids (see Table 7), it is possible to highlight a slight increase in spherical defects for OP3 (quadrants I and II)

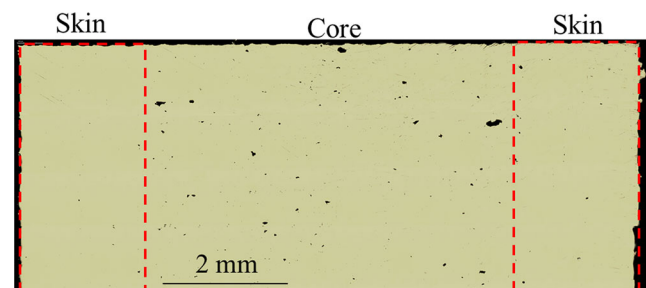
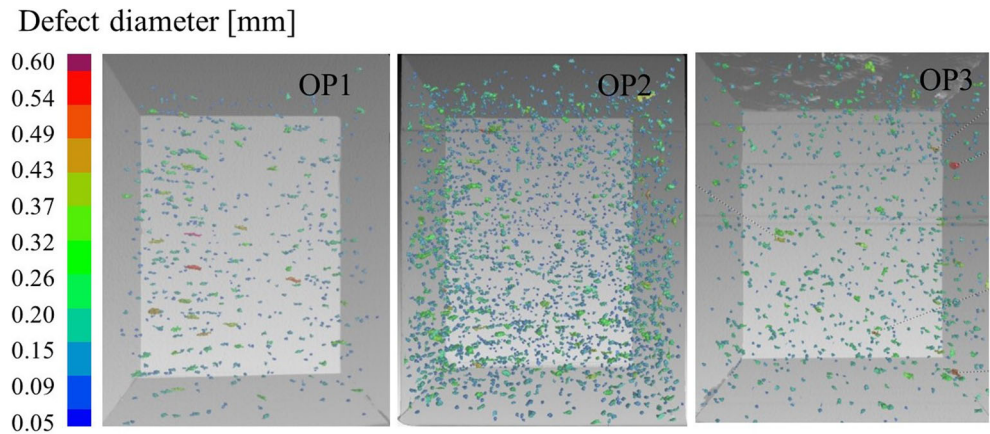


**Fig. 5** Skin and core porosity of the sample

**Fig. 6** CT scan comparison between samples produced with OP1, OP2 and OP3 process parameters



and a noticeable increase in smaller defects (quadrants II and III) with the same parameters. In this comparison, it should be noted that particles with diameters less than 0.05 mm were not identified with the CT scan, so it is probable that gas pores (often smaller than 0.03 mm) were not counted.

Defects with dimension greater than 200 μm developed mainly in the x-y plane (perpendicular to the BD) with a ratio between the z projection and x projection (or y projection) equal to 22–26% (Fig. 9).

Finally, the defect distribution inside OP1 and OP3 samples was compared by dividing the volume into 8 sectors with the same dimensions (3 mm × 3 mm × 4 mm), as shown in Fig. 10.

The percentage of identified voids for each sector is reported in the adjacent table. Defect locations were homoge-

neous in all direction, with an exception connected to the greater presence of pores in sectors IV and VIII of the OP1 sample. By investigating this result, an accumulation of large defects was identified along a specific axis in the z direction. Fig. 11 shows the position of defects with diameters greater than 0.25 mm, with the red ellipse highlighting the recognized aggregation.

However, the involved process parameters were not correlated to this result. This was also confirmed by the distribution of defects detected in OP2 and OP3 samples, which was therefore likely due to the position of the sample on the platform with respect to the direction of the blade and the gas flow.

### 3.3 Mechanical characterization

The tensile properties of as-built AISI 420 components produced with the process parameters given in Table 3 (OP1 and OP2) for three different building directions were measured and compared to those of AISI 420 samples after heat treatments (QT and N+QT). Mean values are reported in Figs. 12 and 13 with the corresponding standard deviation (error bars). Reference values for conventional annealed cold drawn bars and LPBF samples are reported in Table 8.

The influence of process parameters on the mechanical properties of LPBF samples is evident in Fig. 12 on elongation to failure (E %) and UTS, while they have negligible effects on YS. In particular, lower density parameters (OP2) led to a 45–60% reduction in the elongation to failure for all build directions with the higher percentage corresponding to vertical samples, while UTS values decreased by 10–14%. From Fig. 12, it should also be noted that the build direction has a not negligible influence on elongation for both process parameters. Increases in elongation of ~30% were recorded in-plane samples compared to vertical samples for OP1 and ~50% for OP2.

From stereo microscope (Zeiss, Stemi 305) pictures of tensile sample fracture surfaces (Fig. 14), two aspects can be highlight:

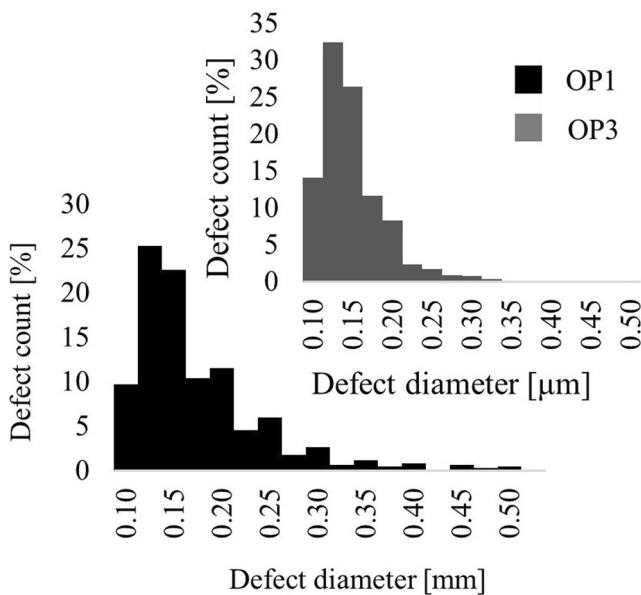
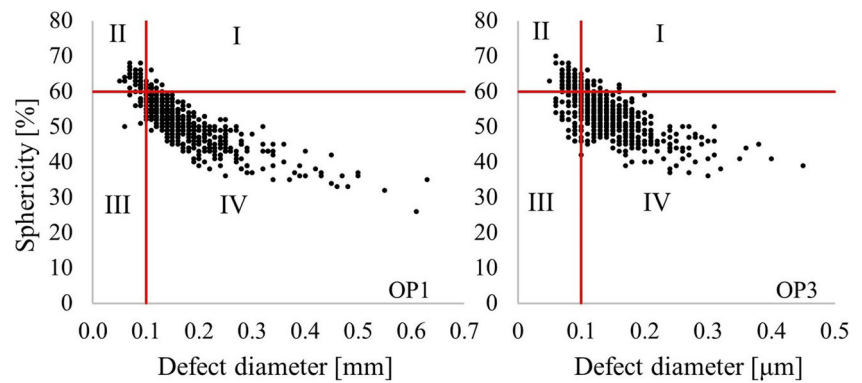


**Fig. 7** Defect count vs defect diameter for OP1 and OP3 samples detected with CT scan

**Fig. 8** Sphericity of defects detected in OP1 (left) and OP3 (right) samples with CT scan at diameters increasing



- Vertical samples (a) fail on a print layer, with the scanning strategy clearly visible on the surface.
- In-plane sample (b), fracture surfaces exhibit a more pronounced necking area confirming the higher elongation behaviour.

In relation to the effect of post-heat treatment on tensile behaviour, Fig. 13 shows an increase in YS and UTS from as-built conditions to heat-treated samples equal to 33% and 12%, respectively, in the case of QT and 33% and 7% in the case of N + QT. The strength increasing due to heat treatment with the formation of tempered martensite with thicker laths (Fig. 15) and the precipitation of carbide from the martensite matrix [12] led to a decrease in elongation, 36% in case of QT and 25% for N+QT.

In order to highlight possible differences in hardness induced by different cooling rates between the upper and lower parts of as-built tensile samples and the differences introduced by the post-heat treatment, Vickers microhardness tests were carried out. Mean values of the aforementioned measurements are shown in Table 9.

Comparing the maximum hardness obtained after bulk heat treatments and laser surface hardening (Fig. 16), the data indicate that the high cooling rate of laser processing allows highest hardness to be achieved (up to ~700 HV). As conventionally occurs for laser hardening, the quenching depth increases with a longer interaction time (lower speed),

**Table 7** Comparison of void geometry between OP1 and OP3 samples

Quadrant	Void geometry	OP1	OP3
I	Diameter > 0.1 mm Sphericity ≥ 60 %	4.0 %	4.5 %
II	Diameter ≤ 0.1 mm Sphericity ≥ 60 %	10.4 %	11.2 %
III	Diameter ≤ 0.1 mm Sphericity < 60 %	5.3 %	12.3 %
IV	Diameter > 0.1 mm Sphericity < 60 %	80.3 %	72 %

responsible for deeper heat conduction. An increase in laser power also corresponds to higher depth, albeit to a lesser extent.

## 4 Discussion

The effect of process parameters and different post-built heat treatments on the density, defect characteristics, hardness, roughness and mechanical properties of martensitic SS (AISI 420) manufactured by LPBF were examined in this paper.

As previously highlighted in other works [23], the heat cycles experienced by the material during LPBF are difficult to predict, and usually the achievement of a selected criterion affects other beneficial properties. Optimization often leads to a compromise between competing requirements. In this work, three sets of parameters, optimized for three specific industrial requirements (higher density, high speed and roughness reduction), were identified.

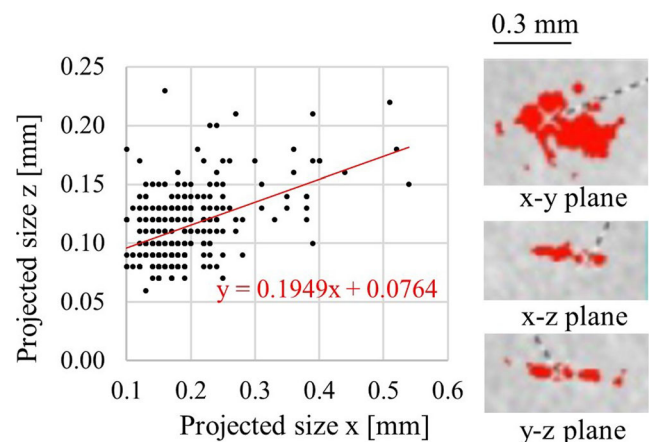


**Fig. 9** Spatial development in x-z plane of OP1 defects with diameter higher than 150 μm (left side) and an example of elongated defect of big dimension (right side)

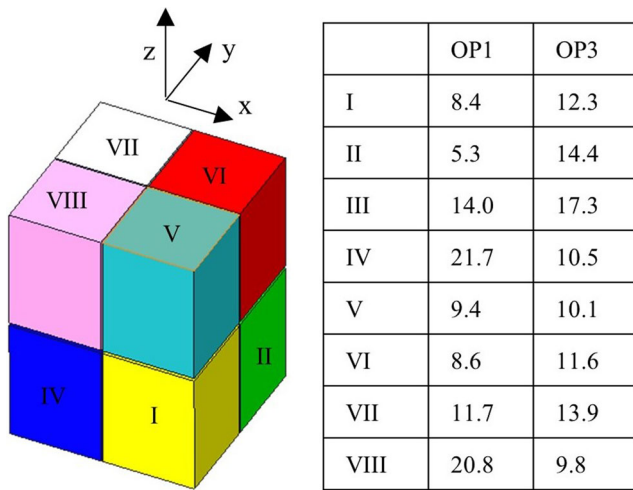


Fig. 10 Defect distribution in terms of percentage terms inside the volume of OP1 and OP3 samples

Starting from this result, the detected defect characteristics were investigated by CT scans. Dimensions, sphericity and distributions of defect in the sample volume were analysed and compared on specimens manufactured with different parameters. Two main categories of defects were recognized.

While morphology is not a conclusive metric for determining the defect formation mechanism, it is reasonable to assume that the first category of defects, including voids with high sphericity (> 60%) and diameters less than 100 μm, formed from insoluble gas bubbles trapped during melt pool resolidification (Fig. 17a, b). The formation of gas porosity is correlated to high peak energy density and in some cases can

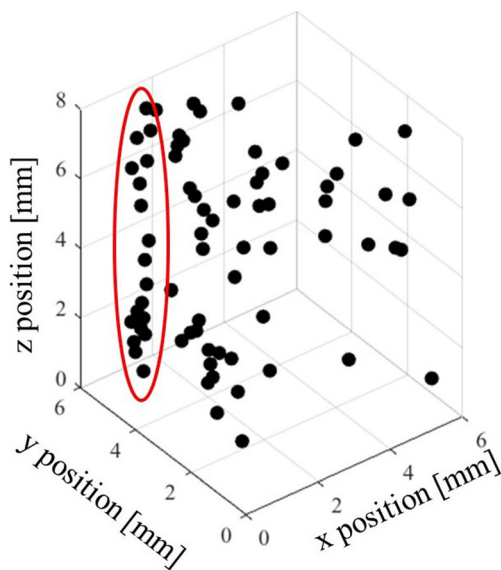


Fig. 11 Large dimension defects accumulation on sectors IV and VIII of OP1 sample

Table 8 Mechanical properties of conventional and LPBF AISI 420 both in as-built and QT condition

	YS [MPa]	UTS [MPa]	E [%]
Conventional [2]	700–750	~800	~18
LPBF as-built [12]	1057±15	1745±27	21.7±3.0
LPBF as-built [11]	700±15	1050±25	2.5±0.2
LPBF as-built [this work]	919–996	1427–1697	2.6–9.7
LPBF QT [12]	1355±36	1945±42	13.4±2
LPBF QT [this work]	1418±14.9	1808±43.2	2.4±0.4

be associated with the presence of a keyhole triggered during powder melting. Keyhole defects, characterized by larger scale spherical pores (usually > 50 μm), are usually associated with high power and low speed. However, recent works suggest that low hatch space, considered in relation to the laser spot diameter, can result in a temperature increasing favouring keyhole formation even with non-conventional parameter combinations [24].

The second group of defects is characterized by larger voids with low sphericity (Fig. 17c, d) and irregular shape. Their presence indicates a lack of energy density or an incorrect relationship between hatch distance, power and laser scan speed [24].

For the parameters investigated by CT, it can be observed that irregular porosity increases with layer thickness, despite the lower scan speed and larger spot diameter. This behaviour agrees with other investigations pointing to low energy density as the primary source of lack of fusion porosity [25].

The irregular void is related to the melt pool boundaries, which may be due to material shrinkage induced by rapid solidification rates. In this case, the void is generated by high residual stresses, which could promote the formation of cracks along melt pool boundaries, leading to final separation and

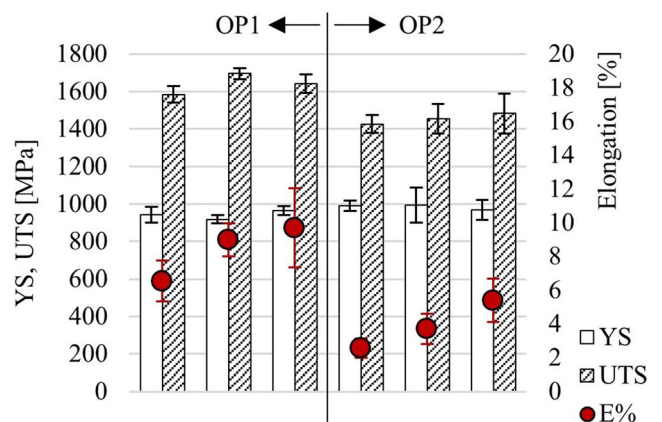
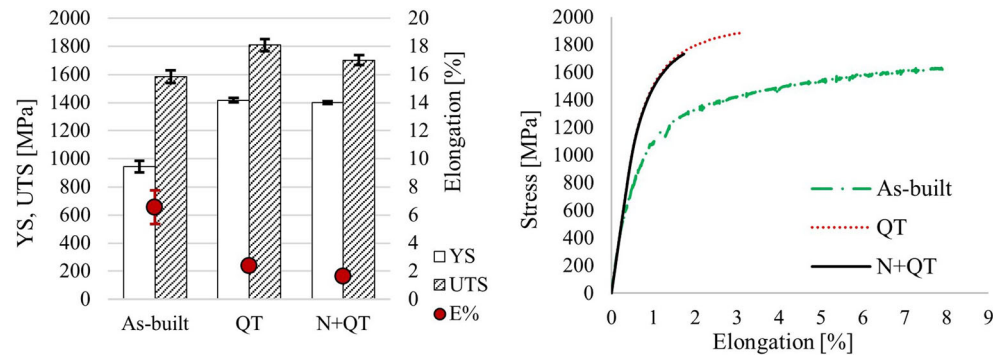


Fig. 12 Mechanical properties of as-built tensile samples

**Fig. 13** Mechanical property comparison between as-built and heat-treated tensile samples



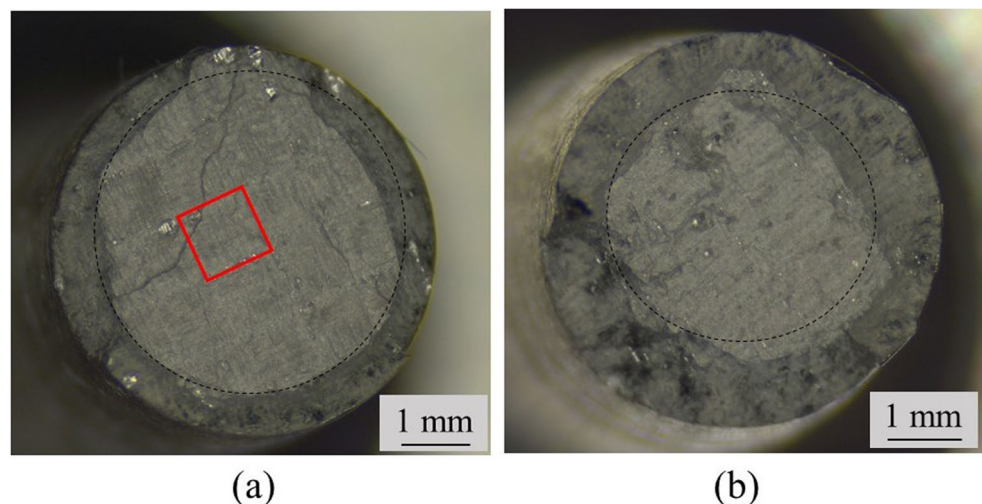
defect formation. The geometry of these defects is often elongated and slender [26], but more spherical defects are not excluded [27]. These defects, as mentioned before, are attributable in part to material shrinkage and for the most part to lack of fusion, as confirmed by microstructural analysis from which it can be observed that elongated voids are formed around unmelted particles (Fig. 17d).

Lack of fusion defects is more dangerous than gas pores in terms of failure, as confirmed by tensile tests. Lower energy density parameters (OP2) are responsible for a reduction in elongation and UTS values. The greater presence of voids and cavities, in fact, strongly reduces material ductility, as has been highlighted before in other studies [27, 28], even due to higher stress concentration [29].

Furthermore, mechanical properties in LPBF parts are strongly influenced by the specific heat cycle involved during the process [30], which cause the typical anisotropy of these components. The hardness results in fact show substantial variations inside as-built samples, for which it is possible to attribute these differences to the height of the specimen. This is confirmed by the

hardness results obtained in the parallelepipeds printed with the same process parameters (Table 9). In this case, the hardness is homogeneous throughout the sample, and the mean value is similar to that measured on the bottom part of the tensile specimen. Higher values of hardness in the top part of the sample, however, differ from what is normally found in the literature [27]. The lower parts of high samples, in fact, are closer to the platform and are subject to higher cooling rates that induce higher hardness values. In the case of AISI 420, the main effect is probably correlated to its response to heat treatments. The increasing hardness of AISI 420 can be attributed to homogenous distribution of lath martensite and an increase in the alloying elements in the austenite due to the higher temperature and soaking time. Excessively high temperatures and time, however, could increase the presence of retained austenite with a detrimental effect on hardness [31]. The obtained hardness data suggest that with the process parameters and heat cycles induced during manufacturing, the beneficial effect of the increase in temperature prevailed over the increase in residual austenite. Differences due to the LPBF heat

**Fig. 14** Failure surface of as-built OP1 samples printed in vertical (a) and in-plane (b) directions



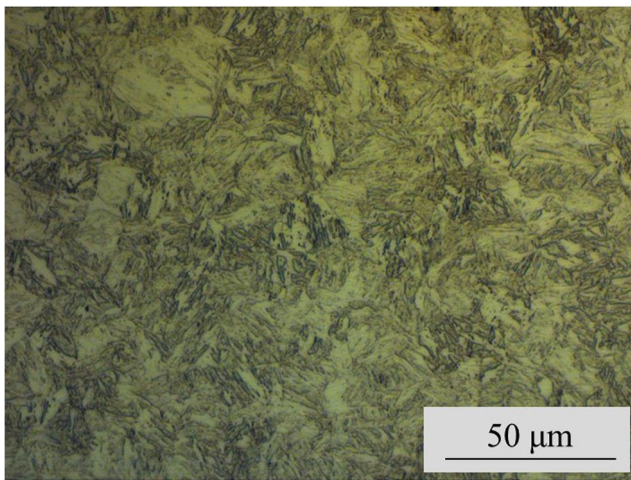


Fig. 15 Optical micrographs of AISI 420 QT sample

cycle have been confirmed by tensile test results on post-heat-treated samples. An increase in strength and hardness together with a decrease in elongation corresponds to martensite.

The obtained results therefore confirm the possibility of identifying LPBF process parameters for martensitic stainless steels suitable to meet the most commonly requested industrial criteria. The effect of these parameters on defect percentage and morphology was examined and correlated with mechanical properties and roughness. The effect of LPBF heat cycle on as-built samples was addressed, and the results of post-heat treatment were shown as a possible solution to prevent anisotropy.

### 5 Conclusion

Based on the results of the conducted analysis, the following conclusions can be drawn:

1. A correlation between the process parameters and the resulting density of LPBF AISI 420 specimens was established, in agreement with the known literature for components manufactured with other steels.

**Table 9** HV0.5 mean values and standard deviation of as-built and heat-treated tensile samples

Sample	HV0.5	Std. dev
OP1, as-built, top	688	60
OP1, as-built, bottom	515	50
OP1, as-built, parallelepiped	527	40
OP1, QT	640	57
OP1, N+QT	633	57

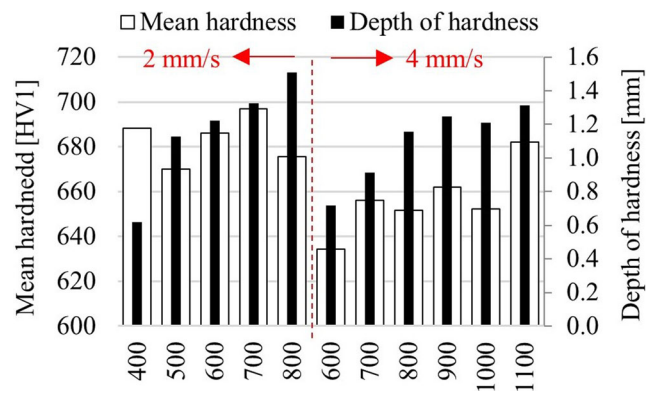


Fig. 16 Mean hardness and quenching depth obtained by laser surface heat treatment at different process parameters

2. Defect differences were observed between samples manufactured with different process parameters. In particular, OP3 samples showed a higher percentage of defects with smaller diameter and a slight increase of spherical defects, but in all conditions, a prevalence of lack of fusion voids was reported.
3. In general, sphericity of defects decreases as the diameter increases, making a distinction between gas porosity and lack of fusion or shrinkage voids possible.
4. Defects with larger dimensions and lower sphericity develop mainly in the x-y plane, perpendicular to the building direction.
5. Defect distributions inside the samples are homogeneous in all directions.
6. In the as-built condition, tensile specimens exhibited similar strength for all build orientations but with

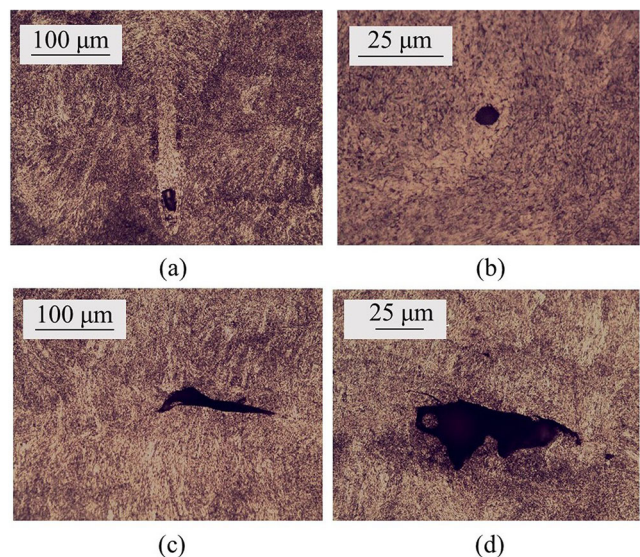


Fig. 17 Main defects detected on OP1 sample. Keyhole gas entrapment (a), gas porosity (b) and lack of fusion (c, d)

increasing elongation from the vertical to in-plane direction, with differences up to 50%.

7. The increasing elongation detected for in-plane samples is due to two aspects: the first is related to the microstructural evolution in LPBF samples, that is, the columnar grain growth in the BD [32]. The second, directly investigated in this paper, is associated with the geometry of lack of fusion defects with projected dimensions that are larger in x-y plane. The tensile load for in-plane samples is orthogonal to the growth direction of microstructural grains and parallel to the direction of defect growth. Both factors improve the elongation, but in OP2 samples, the difference between vertical and in-plane samples is more pronounced due to the greater presence of lack of fusion voids.
8. As-built samples exhibit an ultimate tensile strength of 1697 MPa, yield strength of 996 MPa and elongation of 9.7%. After heat treatment, the strength improved to 1808 MPa and 1418 MPa, respectively, while elongation decreased to 2.4%.
9. Significant differences in hardness (from 515 to 688 HV0.5) were recorded in as-built samples from the bottom to the top as a consequence of the different heat cycles occurring during manufacturing of large components due to differences in heat conduction to the platform, which acts as a heat sink.
10. Greater hardness was measured on heat-treated samples (up to 640 HV0.5), confirming the mechanical behaviour identified with tensile tests. Laser surface hardening, however, achieves the highest hardness (up to 700 HV1) appearing as an interesting alternative for surface property enhancement without resorting to bulk processes.

**Availability of data and material** The datasets analysed during the current study are available from the corresponding author on reasonable request.

**Code availability** Not applicable

**Author contribution** Erica Liverani conceived this research, designed experiments, performed experiments and analysis and wrote the paper; Alessandro Fortunato wrote the paper and participated in the revisions of it. All authors read and approved the final manuscript.

**Funding** Open access funding provided by Alma Mater Studiorum - Università di Bologna within the CRUI-CARE Agreement.

## Declarations

**Ethics approval** Not applicable

**Consent to participate** Not applicable

**Consent for publication** Not applicable

**Conflict of interest** The authors declare no competing interests.

**Additional declarations for articles in life science journals that report the results of studies involving humans and/or animals** Not applicable

**Open Access** This article is licensed under a Creative Commons Attribution 4.0 International License, which permits use, sharing, adaptation, distribution and reproduction in any medium or format, as long as you give appropriate credit to the original author(s) and the source, provide a link to the Creative Commons licence, and indicate if changes were made. The images or other third party material in this article are included in the article's Creative Commons licence, unless indicated otherwise in a credit line to the material. If material is not included in the article's Creative Commons licence and your intended use is not permitted by statutory regulation or exceeds the permitted use, you will need to obtain permission directly from the copyright holder. To view a copy of this licence, visit <http://creativecommons.org/licenses/by/4.0/>.

## References

1. Escobar JD, Poplawsky JD, Faria GA, Rodriguez OJP, Salvador CAF, Mei PR, Babu SS, Ramirez AJ (2018) Compositional analysis on the reverted austenite and tempered martensite in a Ti-stabilized supermartensitic stainless steel: Segregation, partitioning and carbide precipitation. *Mater Des* 140:95–105. <https://doi.org/10.1016/j.matdes.2017.11.055>
2. Fayazfar H, Salarian M, Rogalsky A, Sarker D, Russo P, Paserin V, Toyserkani E (2018) A critical review of powder-based additive manufacturing of ferrous alloys: process parameters, microstructure and mechanical properties. *Mater Des* 144:98–128. <https://doi.org/10.1016/j.matdes.2018.02.018>
3. Brnic J, Turkalj G, Canadija M, Lanc D, Krscanski S (2011) Martensitic stainless steel AISI 420-mechanical properties, creep and fracture toughness. *Mech Time-Depend Mater* 15:341–352. <https://doi.org/10.1007/s11043-011-9137-x>
4. Alam MK, Mehdi M, Urbanic RJ, Edrisky A (2020) Mechanical behavior of additive manufactured AISI 420 martensitic stainless steel. *Mat Sci Eng: A* 773:138815. <https://doi.org/10.1016/j.msea.2019.138815>
5. Krakhmalev P, Yadroitsava I, Fredriksson G, Yadroitsev I (2015) In situ heat treatment in selective laser melted martensitic AISI 420 stainless steels. *Mater Des* 87:380–385. <https://doi.org/10.1016/j.matdes.2015.08.045>
6. Yadollahi A, Shamsaei N (2017) Additive manufacturing of fatigue resistant materials: challenges and opportunities. *Int J Fatigue* 98: 14–31. <https://doi.org/10.1016/j.ijfatigue.2017.01.001>
7. Tyagi P, Goulet T, Riso C, Stephenson R, Chuenprateep N, Schlitzer J, Benton C, Garcia-Moreno F (2019) Reducing the roughness of internal surface of an additive manufacturing produced 316 steel component by chempolishing and electropolishing. *Additiv Manu* 25:32–38. <https://doi.org/10.1016/j.addma.2018.11.001>
8. Fox JC, Moylan SP, Lane BM (2016) Effect of process parameters on the surface roughness of overhanging structures in laser powder bed fusion additive manufacturing. *Procedia CIRP* 45:131–134. <https://doi.org/10.1016/j.procir.2016.02.347>

9. Ravi GA, Hao XJ, Wain N, Wu X, Attallah MM (2013) Direct laser fabrication of three dimensional components using SC420 stainless steel. *Mater Des* 47:731–736. <https://doi.org/10.1016/j.matdes.2012.12.062>
10. Zhao X, Wei Q, Song B, Liu Y, Luo X, Wen S, Shi Y (2015) Fabrication and characterization of AISI 420 stainless steel using selective laser melting. *Mater Manu Processes* 30(11):1293–1289. <https://doi.org/10.1080/10426914.2015.1026351>
11. Saeidi K, Zapata DL, Lofaj F, Kvetkova L, Olsen J, Shen Z, Akhtar F (2019) Ultra-high strength martensitic 420 stainless steel with high ductility. *Additiv Manu* 29:100803. <https://doi.org/10.1016/j.addma.2019.100803>
12. Nath SD, Irrinki H, Gupta G, Kearns M, Gulsoy O, Atre S (2019) Microstructure-property relationships of 420 stainless steel fabricated by laser-powder bed fusion. *Powder Technol* 343:738–746. <https://doi.org/10.1016/j.powtec.2018.11.075>
13. Tian Y, Chadha K, Aranas C (2021) Laser powder bed fusion of ultra-high-strength 420 stainless steel: microstructure characterization, texture evolution and mechanical properties. *Mater Sci Eng A* 805:140790
14. Esmaeilzadeh R, Keshavarzkermani A, Ali U, Behravesht B, Bonakdar A, Jahed H, Toyserkani E (2021) On the effect of laser powder-bed fusion process parameters on quasi-static and fatigue behaviour of Hastelloy X: a microstructure/defect interaction study. *Additiv Manu* 38:101805. <https://doi.org/10.1016/j.addma.2020.101805>
15. Kale AB, Choi SH, Kim BK, Kim DI, Castle EG, Reece M (2020) An investigation of the corrosion behavior of 316L stainless steel fabricated by SLM and SPS techniques. *Mater Charact* 163:110204. <https://doi.org/10.1016/j.matchar.2020.110204>
16. Smith J, Xiong W, Yan W, Lin S, Cheng P, Kafka OL, Wagner GJ, Cao J, Liu WK (2016) Linking process, structure, property, and performance for metal-based additive manufacturing: computational approaches with experimental support. *Comput Mech* 57:583–610. <https://doi.org/10.1007/s00466-015-1240-4>
17. Moradi M, Arabi H, Nasab SJ, Benyounis KY (2019) A comparative study of laser surface hardening of AISI 410 and 420 martensitic stainless steels by using diode laser. *Opt Laser Technol* 111:347–357. <https://doi.org/10.1016/j.optlastec.2018.10.013>
18. Spierings AB, Schneider M (2011) Comparison of Density measurement techniques for additive manufactured metallic parts. *J. Rapid Prototyping* 17(5):380–386. <https://doi.org/10.1108/13552541111156504>
19. Sanaei N, Fatemi A, Phan N (2019) Defect characteristics and analysis of their variability in metal L-PBF additive manufacturing. *Mater Des* 182:108091. <https://doi.org/10.1016/j.matdes.2019.108091>
20. ISO Standard. ISO 6892-1 Metallic materials - tensile testing, part 1: method of test at room temperature
21. Guo C, Li S, Shi S, Li X, Hu X, Zhu Q, Ward RM (2020) Effect of processing parameters on surface roughness, porosity and cracking of as-built IN738LC parts fabricated by laser powder bed fusion. *J Mater Process Technol* 285:116788. <https://doi.org/10.1016/j.jmatprotec.2020.116788>
22. Tian Y, Tomus D, Rometsch P, Wu X (2017) Influences of processing parameters on surface roughness of Hastelloy X produced by selective laser melting. *Additive Manufacturing* 13:103–112. <https://doi.org/10.1016/j.addma.2016.10.010>
23. Oliveira JP, Ma J, LaLonde AD (2020) Processing parameters in laser powder bed fusion metal additive manufacturing. *Mater Des* 193:108762. <https://doi.org/10.1016/j.matdes.2020.108762>
24. Gordon JV, Narra SP, Cunningham RW, Liu H, Chen H, Suter RM, Beuth JL, Rollett AD (2020) Defect structure process maps for laser powder bed fusion additive manufacturing. *Additive Manufacturing* 36:101552. <https://doi.org/10.1016/j.addma.2020.101552>
25. Gong H, Rafi K, Gu H, Starr T, Stucker B (2014) Analysis of defect generation in Ti-6Al-4V parts made using powder bed fusion additive manufacturing processes. *Additive Manufacturing* 1:87–98. <https://doi.org/10.1016/j.addma.2014.08.002>
26. Zhou Z, Huang L, Shang Y, Li Y, Jiang L, Lei Q (2018) Causes analysis on cracks in nickel-based single crystal superalloy fabricated by laser powder deposition additive manufacturing. *Mater Des* 160:1238–1249. <https://doi.org/10.1016/j.matdes.2018.10.042>
27. Liverani E, Toschi S, Ceschini L, Fortunato A (2017) Effect of selective laser melting (SLM) process parameters on microstructure and mechanical properties of 316L austenitic stainless steel. *J Mater Process Technol* 249:255–263. <https://doi.org/10.1016/j.jmatprotec.2017.05.042>
28. Olakanmi EO, Cochrane RF, Dalgarno KW (2015) A review on selective laser sintering/melting (SLS/SLM) of aluminium alloy powders: processing, microstructure, and properties. *Prog Mater Sci* 74:401–477. <https://doi.org/10.1016/j.pmatsci.2015.03.002>
29. Xie C, Wu S, Yu Y, Zhang H, Hu Y, Zhang M, Wang G (2021) Defect-correlated fatigue resistance of additively manufactured Al-Mg4.5Mn alloy with in situ micro-rolling. *J Mater Process Technol* 291:117039. <https://doi.org/10.1016/j.jmatprotec.2020.117039>
30. Charmi A, Falkenberg R, Ávila L, Mohr G, Sommer K, Ulbricht A, Sprengel M, Saliwan Neumann R, Skrotzki B, Evans A (2021) Mechanical anisotropy of additively manufactured stainless steel 316L: an experimental and numerical study. *Mater Sci Eng A* 799:140154. <https://doi.org/10.1016/j.msea.2020.140154>
31. Nasery Isfahany A, Saghafian H, Borhani G (2011) The effect of heat treatment on mechanical properties and corrosion behavior of AISI420 martensitic stainless steel. *J Alloys Compounds* 509(9):3931–3936. <https://doi.org/10.1016/j.jallcom.2010.12.174>
32. Tonelli L, Ceschini L, Fortunato A (2020) CoCr alloy processed by selective laser melting (SLM): effect of laser energy density on microstructure, surface morphology, and hardness. *J Manuf Process* 52:106–119. <https://doi.org/10.1016/j.jmapro.2020.01.052>

**Publisher's note** Springer Nature remains neutral with regard to jurisdictional claims in published maps and institutional affiliations.